

Designing heterostructures to control oxygen stoichiometry in helimagnetic perovskite strontium ferrite

J. Fowlie,^{1,2,3} B. Mundet,⁴ D. Puggioni,³ L. Bhatt,⁵ E. R. Hoglund,⁶ W. J. Kim,^{1,2,7} J. Li,^{1,2} S. J. Lee,⁸ W. Liu,³ A. Devinenti,³ J. M. Rondinelli,³ D. A. Muller,^{5,9} and H. Y. Hwang^{1,2}

¹Stanford Institute for Materials and Energy Sciences, SLAC National Accelerator Laboratory, Menlo Park, CA 94025, USA

²Department of Applied Physics, Stanford University, Stanford, CA 94305, USA

³Department of Materials Science and Engineering, Northwestern University, Evanston, 60208, USA

⁴Catalan Institute of Nanoscience and Nanotechnology (ICN2), Barcelona 08193 Catalonia, Spain

⁵School of Applied and Engineering Physics, Cornell University, Ithaca, New York, 14850, USA

⁶Center for Nanophase Materials Sciences, Oak Ridge National Laboratory, Oak Ridge, TN, 37830, USA

⁷Department of Material Science Engineering, Pusan National University, Busan 46241, Republic of Korea

⁸Stanford Synchrotron Radiation Lightsource, SLAC National Accelerator Laboratory, Menlo Park, CA 94025, USA

⁹Kavli Institute at Cornell for Nanoscale Technology, Cornell University, Ithaca, New York, 14850, USA

(*Electronic mail: jfowlie@northwestern.edu.)

(Dated: 26 February 2026)

A large challenge in determining the physics of helimagnetic SrFeO₃ is in stabilizing the stoichiometric chemical phase over long enough time scales to conduct extensive measurements. Degradation in SrFeO₃ manifests mainly as a crossover from metallic to insulating behavior. Using a combination of electronic transport and density functional theory, we show that this degradation is dominated by oxygen loss, possibly on the order of one percent. We further demonstrate that high quality SrFeO₃ thin films can be stabilized long-term by combining a nanoscale band insulator capping layer with an *ex situ* ozone anneal. We show that this produces a nearly-pristine cation sublattice and preserves metallicity for at least several weeks. These results establish a reliable pathway for producing chemically stable SrFeO₃ thin films, enabling reproducible studies of its unusual helimagnetism.

I. INTRODUCTION

Perovskite SrFeO₃ is an unusual example of a helimagnetic compound that is centrosymmetric and cubic, so its helimagnetism cannot be explained by Dzyaloshinskii-Moriya physics or by frustration¹⁻³. Helimagnetism, and topologically-protected magnetic structures that are reported in this compound³, also make SrFeO₃ an interesting material in the context of spintronic, magnonic, qubit, and high-density memory applications^{4,5}.

One of the primary impediments to the further study of helimagnetism in SrFeO₃ is that the compound is metastable at ambient conditions. This metastability is believed to be driven by the relatively unfavorable Fe⁴⁺ valence state and its tendency to reduce toward Fe³⁺. This leads to two challenges: (1) as-grown SrFeO₃ is usually reported to be oxygen deficient SrFeO_{3- δ} ^{6,7}, and (2) SrFeO₃ (or SrFeO_{3- δ}) will rapidly degrade (further), preventing reliable characterization, especially multi-probe, at large facilities, or over an extended period of time^{8,9}.

Although a hindrance to studies of electronic and magnetic properties, this evolution in oxygen stoichiometry has brought much recent attention to SrFeO₃ because it facilitates superior oxygen-ion transport properties for potential application in nonvolatile neuromorphic hardware^{10,11}. In particular, electric

field is found to drive a reversible phase transition between the perovskite phase and the brownmillerite SrFeO_{2.5}¹¹. Such a transition involves only the movement of oxygen anions and can be considered as a topotactic redox reaction, where topotactic refers to the fact that the arrangement of the cation sublattice remains the same.

Precise control of the oxidation state of SrFeO_x and, in particular, preventing the fully oxidized SrFeO₃ from degrading, has yet to be demonstrated. Here we report the positive effect of a nanometric band insulator capping layer on the transport and microstructure properties of SrFeO_x thin films. Such a capping layer produces the highest quality SrFeO₃ reported to date, provides evidence that the nature of the degradation is indeed oxygen loss and is reversible, and stabilizes high quality SrFeO₃ over many weeks, enabling extensive investigation of electronic and magnetic properties¹².

II. RESULTS

1. Growth and characterization

Epitaxial thin films of strontium ferrite were grown on pseudocubic perovskite (LaAlO₃)_{0.3}(Sr₂AlTaO₆)_{0.7} (LSAT) single crystal substrates terminated on the (001) plane¹³. When used,

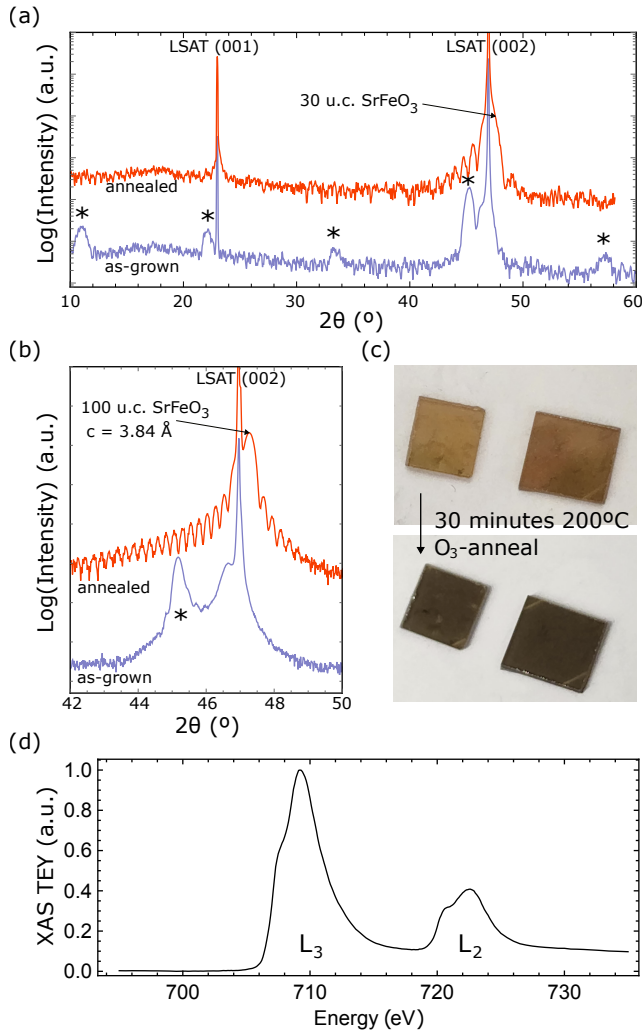


FIG. 1. (a) $\theta - 2\theta$ x-ray diffraction scans of a 30 u.c. (11 nm) SrFeO_x thin film with a 4 u.c. (1.6 nm) capping layer of SrTiO_3 before (blue) and after (red) ozone anneal. (b) $\theta - 2\theta$ scans before and after annealing for a 100 u.c. (38 nm) sample with a 3 u.c. (1.2 nm) capping layer of SrTiO_3 . Asterisks indicate the peaks characteristic of the brownmillerite phase. (c) Photograph of two SrFeO_x samples before and after ozone-annealing. (d) X-ray absorption in total electron yield around the Fe $L_{2,3}$ edges of a fully oxidized SrFeO_3 film.

an epitaxial capping layer of SrTiO_3 was grown on top. LSAT, with a lattice parameter of 3.87 \AA , provides a tensile strain of $+0.5 \%$ to perovskite SrFeO_3 , which has a bulk lattice parameter of 3.85 \AA ^{1,14,15}. Further details on the sample growth by pulsed laser deposition (PLD) are given in the Methods Section. As grown, the films are brownmillerite $\text{SrFeO}_{2.5}$ or oxygen-deficient perovskite $\text{SrFeO}_{3-\delta}$ rather than SrFeO_3 . Unless otherwise stated, all films were topotactically oxidized by an *ex situ* post-anneal in ozone, described in the Methods section. Fig. 1(a) and (b) show $\theta - 2\theta$ scans of the strontium ferrite films as grown (lower curves in each plot) and after the ozone anneal (upper curves in each plot). In both thin (30 u.c. or 11 nm) and thick (100 u.c. or 38 nm) films, there is a complete phase transformation from brownmillerite (peaks

indicated by asterisks) to perovskite. Finite thickness fringes indicate the high quality of the perovskite phase. Fig. 1(c) is an optical photograph of strontium ferrite samples before (top) and after (bottom) ozone-annealing. The color change is due to the transformation from an insulator to a metal.

Fig. 1(d) shows the $\text{Fe}_{2,3}$ x-ray absorption edge spectrum recorded in total electron yield for an 11 nm film of SrFeO_3 after standard ozone annealing. The features observed on both edges are consistent with an iron valence state, or oxidation state, of $4+$ ¹⁶.

2. Electronic transport

Fig. 2(a) shows typical resistivity data as a function of temperature for a 12 nm thick film of SrFeO_3 on LSAT (001) substrate with a 1.6 nm SrTiO_3 capping layer. The resistive anomalies indicate Néel transitions between phases of distinct helimagnetic order and have been labeled according to the established convention². Residual resistivity is around $100 \mu\Omega\text{cm}$ and the residual resistivity ratio is around 6. Based on these quantifications of metallicity, we suggest that our SrFeO_3 is the highest quality reported to date among all growth methods (single crystal, powder, molecular beam epitaxy and pulsed laser deposition) and all *ex* and *in situ* oxidation processes (solid oxidizer, oxygen, and ozone)^{2,8,9,14,17–22}. Table S1 in the Supplementary Material (SM) summarizes a comparison with prior reports. The high quality of our samples also manifests in the sharpness of the resistive transitions, particularly the transition between Phase I and II, which is often observed as a broad hysteresis in literature. We suggest that the capping layer enhances the quality of our SrFeO_3 evidenced in electronic transport.

Consistent with previous reports^{8,9}, the metallicity of bare SrFeO_3 degrades rapidly with time. This is shown in Fig. 2(b) for an 11 nm SrFeO_3 film freshly annealed in ozone. The aging of the sample takes place at room temperature in air. Notably, the black curve evolves to the blue curve after only six hours, at which point the resistivity has doubled and the lower temperature Phase I-Phase II Néel transition is no longer discernible. After 16 days the transport behavior is insulating and the resistivity approaches $0.1 \Omega\text{cm}$. After a reanneal in ozone, the metallicity can be returned (red curve), supporting the assertion that the degradation is due to oxygen loss. We note that, although the residual resistivity rises upon reannealing (compared to initial anneal), the residual resistivity ratio is quite similar.

Fig. 2(c) displays four resistivity curves, corresponding to the same aging periods as the data in panel (b), but here the 11 nm film of SrFeO_3 is capped with 1.6 nm of SrTiO_3 . The curves are indistinguishable. Thus, the degradation of the metallicity of SrFeO_3 can be prevented by the addition of a thin capping layer of SrTiO_3 .

Extended time-dependent low temperature resistivity data are plotted in Fig. 2(d) where it is clear that even a SrTiO_3 capping layer of less than 1 nm in thickness is sufficient to maintain the metallicity of SrFeO_3 over weeks.

Previous work by Enriquez *et al* has shown that a 300 nm

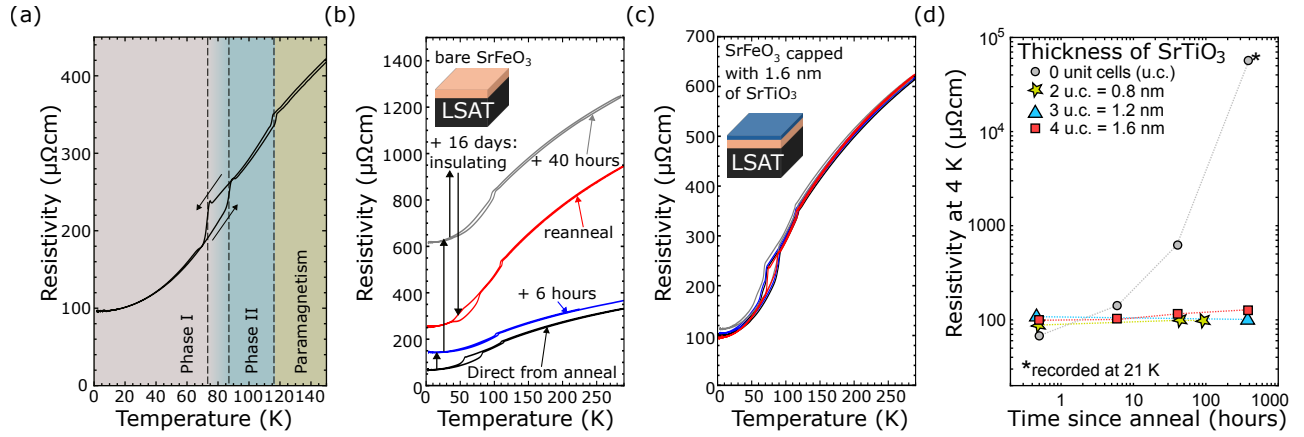


FIG. 2. (a) Low temperature close-up of the resistive transitions of SrFeO_3 , labeled in accordance with Ishiwata *et al.*². (b) Resistivity as a function of temperature showing degradation of the metallicity of bare SrFeO_3 over several hours. Metallicity is returned after a repeat ozone anneal. (c) With a thin SrTiO_3 capping layer, the metallicity is retained over many hours. The four resistivity versus temperature curves, with the same color coding as in panel (b), are almost indistinguishable. (d) Log-log plot of the time dependence, over several weeks, of the 4 K resistivity of SrFeO_3 with different thicknesses of capping layer. Dashed lines are guides to the eye. The asterisk marks one data point that was recorded at 21 K due to the resistivity exceeding the measurement limit at lower temperatures.

capping layer of amorphous Al_2O_3 maintains a constant resistivity of already oxygen-deficient $\text{SrFeO}_{3-\delta}$ over several days⁹. Our result is a significant improvement for two reasons. First, the *ex situ* ozone anneal can be performed with the SrTiO_3 cap because we propose that it is thin enough to allow oxygen to diffuse into the sample at the $\approx 200^\circ\text{C}$ temperatures at which the annealing takes place but it is thick enough that the oxygen cannot diffuse out again at room temperature. This “valve”-like functionality allows us to achieve the high quality metallicity of fully oxidized SrFeO_3 that we show in Fig. 2(a). A much thicker cap would be too great of a diffusion barrier for complete oxidation. Second, a capping layer of less than 1 nm in thickness does not impede measurement, with the exception of only the most surface-sensitive techniques.

Like Enriquez and coworkers, we believe that the observed degradation of metallicity in SrFeO_3 is due to oxygen loss as the iron strives to return to the energetically more favorable Fe^{3+} valence state. The effect of the capping layer and the renewed metallicity upon reannealing are our first pieces of evidence.

3. First principles calculations

To gain further insight into the high sensitivity of conductivity to oxygen loss we carry out first principles density functional theory (DFT) calculations. The band structure of pristine SrFeO_3 reveals three hole-like bands at the A point with a finite density of states at the Fermi level, see Fig. 3(a). Upon increasing oxygen vacancies to 1.7%, these bands shift to lower energy until their band maximum aligns with the Fermi level, see Fig. 3(b). At 3.3% oxygen vacancies, these bands no longer intersect with the Fermi level and any carriers they contribute are frozen out. With on order 1% oxygen vacancies we, therefore, expect a significant decrease in electronic conductivity,

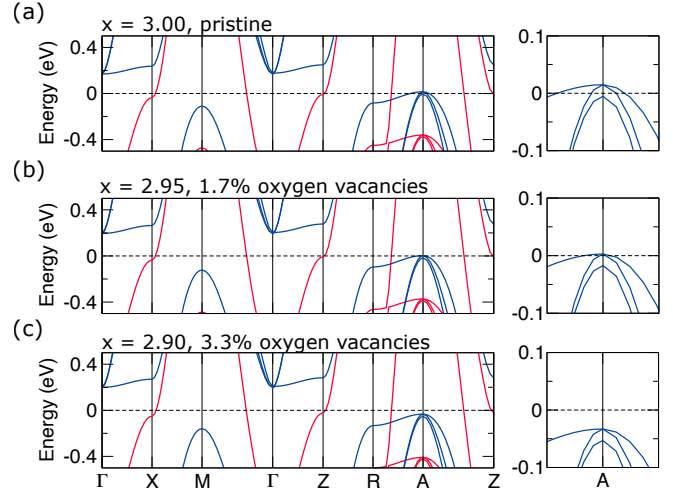


FIG. 3. Computed band structure of SrFeO_x with $x = 3.0$ (a), $x = 2.95$ (b) and $x = 2.9$ (c). Red and blue bands denote spin up and spin down respectively. Panels on the right display a close-up view around the Fermi level at the A-point.

consistent with our resistivity data shown in Fig. 2).

We note that X-ray diffraction does not show a significant change in the film peak position in 2θ over the course of the metallicity degradation, as shown in the SM Fig. S1. This may be because oxygen loss on the scale modeled by our DFT is too small to result in a significant expansion of the lattice parameter. It may also be because SrFeO_3 is metallic and is able to locally screen the distribution of oxygen vacancies.

Our first principles calculations lend support to our conclusion that oxygen loss is the source of the degradation of metallicity of SrFeO_3 and, furthermore, that the off-stoichiometry may only be on the order of one percent.

4. Transmission electron microscopy

Recently, Wang and coworkers suggest that the metallicity degradation in SrFeO₃ has a contribution from extended defects in the cation sublattice that they describe as strontium-rich nanogaps⁸. They observe these nanogaps in SrFeO₃ grown on different substrates, including LSAT. The nanogaps, which they further suggest are a strain relaxation mechanism, are not observed in our samples, as evidenced by our scanning transmission electron microscopy (STEM) analysis.

Fig. 4 shows a series of low magnification high angle annular dark field (HAADF) images. Note that ozone annealing fully oxidizes the films to produce perovskite SrFeO₃, as evidenced by x-ray diffraction, but either the focused ion beam to prepare the STEM lamella, or the electron beam in the microscope, further reduce the film back to brownmillerite. This is a known challenge in SrFeO₃²³. Reduction of SrFeO_{2.5} to the infinite-layer SrFeO₂ has also been observed under the electron beam during STEM imaging, as we show in SM Fig. S2, and has been reported by others²⁴. Therefore, beam-induced oxygen loss, as observed in many oxides²⁵, is not unprecedented in strontium ferrite.

Fig. 4 (a) shows a STEM image of a standard, 11 nm as-grown (before ozone anneal) SrFeO_{2.5} sample with a 1.6 nm SrTiO₃ capping layer. The dark bands in the image represent the oxygen vacancy channels of the brownmillerite SrFeO_{2.5}. Crucially, the strontium-iron cation sublattice is an interpenetrating primitive cubic lattice with negligible extended defects.

To address the possibility that the addition of the SrTiO₃ capping layer prevents the formation of extended cation defects, we also perform STEM analyses on an uncapped as-grown SrFeO_{2.5} sample, as shown in Fig. 4 (b). As before, the narrow dark bands in the HAADF image are the oxygen vacancy channels of the brownmillerite structure. There is an additional, wider, dark band close to the substrate (indicated by the red arrows on either end). This is a rocksalt-like antiphase cation defect, yet distinct from the denser and more significant extended defects observed by Wang *et al*⁸.

To exclude the possibility that Sr-rich nanogaps form only during the oxidizing process, we perform STEM imaging on *annealed* samples that were, before annealing, equivalent to those shown in Fig. 4(a) and (b). In the capped sample (c) no extended defects are observed and the cation sublattice is pristine. In the uncapped sample (d) we observe the same extended defect near the interface as in the as-grown counterpart but no other defects.

We also note that regions of vertical oxygen vacancy channels are observed in many samples, with and without capping layer. The coexistence of both orientations of brownmillerite structure, as well as the low energy barrier to switch between them, has been observed previously²⁶.

Finally, Fig. 4 (e) and (f) display the electron energy loss spectroscopy (EELS) and energy dispersive x-ray spectroscopy (EDX) maps, respectively, for the same as-grown sample as in Fig. 4(a). With this element specificity, we have further verified that the cation sublattice is close to pristine in this sample.

We therefore suggest that, while the degradation of metallicity in SrFeO₃ without a capping layer is ubiquitous, the

development of extended cation defects, e.g., strontium-rich nanogaps, is not. While the SrFeO₃ films are not defect-free, particularly when there is no capping layer, the relative sparseness of the defects, as well as their general orientation in the plane, cannot explain the increase in resistivity of orders of magnitude that we observe in Fig. 2(b).

III. DISCUSSION AND CONCLUSION

We have demonstrated that the degraded metallicity of SrFeO₃ can be explained by oxygen stoichiometry only. While it is challenging to quantify the level of oxygen loss, we deduce that it is not a large change because no shift in the x-ray diffraction peak is observed to correspond to the degraded metallicity (Fig. S1 in SM). This is supported by our DFT calculations, which show that a loss of oxygen of only $\approx 1.7\%$ results in the depletion of the small A-centered hole pocket at the Fermi level. We believe that the strong negative charge transfer character of SrFeO₃ plays an important role²⁷. Nominally d⁴, a significant portion of the oxygen 2p electrons are transferred to the iron, making the electronic configuration closer to d⁵L where L denotes a ligand hole^{21,28,29}. The relevance of oxygen states at the Fermi level leads to the strong sensitivity of resistivity to oxygen content.

Further supporting our conclusion that oxygen loss alone is responsible for degraded metallicity in SrFeO₃, our STEM imaging shows a close-to-pristine cation sublattice with and without a capping layer, and with and without ozone annealing.

As a materials synthesis strategy, we have shown that a thin, less than 1 nm, capping layer of band insulator SrTiO₃ is thin enough to allow complete oxidation of the underlying ferrite, while being sufficiently thick to retain metallicity over several weeks. As shown in SM Fig. S3, our capped SrFeO₃ does not exhibit significant degradation until around 100 °C. Previous work on SrVO₃, which has a tendency to gain oxygen, has found amorphous capping layers of 4 - 10 nm thickness to be effective in retaining the stoichiometry^{30,31}. A 6 u.c. (2.4 nm) crystalline SrTiO₃ capping layer has previously shown potential in stabilizing Mo⁴⁺ molybdates over 5 minutes up to 450 °C³². Those authors claim that the continuity of the transition metal valence at the interface with SrTiO₃ (Ti⁴⁺-Mo⁴⁺) may help the stability, which would also be true in the case of SrFeO₃ (Ti⁴⁺-Fe⁴⁺). We propose that the stability of our system is further enhanced by the compressive strain of -0.9% that the SrTiO₃ experiences due to the epitaxial relationship with the LSAT substrate, transmitted through the SrFeO₃ film. There is evidence that tensile strain promotes oxygen diffusion in perovskite oxides while compressive strain suppresses it^{33,34}. Amorphous capping layers and tensile strained or relaxed crystalline capping layers may, therefore, be less effective than the compressively-strained crystalline capping layer of SrTiO₃ that we use here.

We also show that metallicity can be returned with a repeat ozone anneal. This will enable more intensive, multi-modal measurements of SrFeO₃, and may be generalizable to other oxides with an unfavorable valence state.

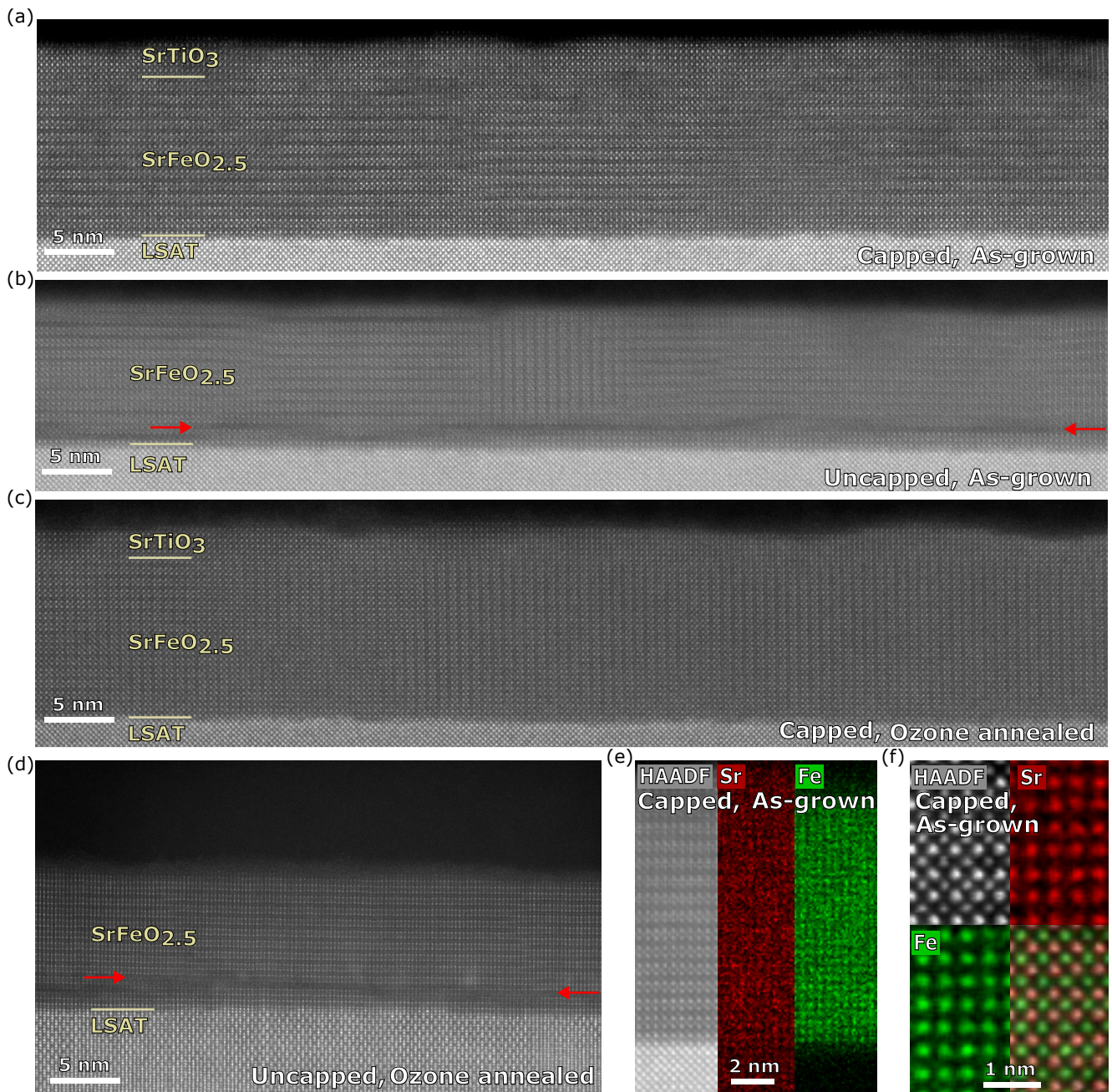


FIG. 4. (a) Low magnification high angle annular dark field (HAADF) image of an 11 nm thick film of as-grown SrFeO_{2.5} with a 1.6 nm SrTiO₃ cap. (b) Low magnification HAADF image of an 11 nm as-grown SrFeO_{2.5} film with no capping layer. One horizontal fault in the cation sublattice can be identified and is marked with red arrows. (c) Low magnification HAADF image of an 11 nm thick film of SrFeO_{2.5} with a 1.6 nm SrTiO₃ capping layer after having been ozone annealed. (d) Low magnification ADF image of the same film as in (b) after having been ozone annealed. The cation fault is indicated by red arrows. Both ozone annealed samples in (c) and (d) were initially SrFeO₃ and reduced unintentionally by the ion beam or electron beam to SrFeO_{2.5}. In all HAADF images the chemical interfaces are marked by yellow bars. (e) On the left a high magnification image of the same sample as in (a) with the electron energy loss spectroscopy (EELS) signal of strontium (middle) and iron (right) taken from the same region. (f) Energy-dispersive x-ray spectroscopy (EDX) maps in a small region of the same sample as in (a) and (e). The combined EDX signals of strontium and iron is shown in the lower right panel.

IV. SUPPLEMENTARY MATERIAL

A Supplementary Material (SM) file is available. The file contains a quantitative comparison of metallicity between

SrFeO₃ samples reported in literature, evidence that the *c*-axis lattice parameter is not significantly affected by low levels of oxygen loss, further STEM images demonstrating the reduction to infinite-layer SrFeO₂ and an experiment upon heating

capped SrFeO_x in air on a hot plate suggesting that oxygen loss is insignificant up to 100 °C.

V. METHODS

Sample preparation

Thin film samples were grown by pulsed laser deposition by a KrF excimer laser of 248 nm wavelength operating at 3 Hz. The laser fluence was calculated to be 0.97 J cm⁻². The target was a pressed powder of SrFeO_{2.5}. All samples reported in this work were grown in 50 mTorr of flowing oxygen at 620 °C, as measured by a pyrometer detecting the front side of the substrate. SrTiO₃ capping layers were grown *in situ* at the same conditions as, and immediately following, SrFeO_{2.5}. A single crystal of SrTiO₃ served as the target. Warm up and cool down were ramps of 100 °C per minute and were carried out in the same oxygen partial pressure as the growth. *Ex situ* ozone anneal was performed at 180 - 260 °C for 0.5 to 3 hours in a UV-assisted ozone plasma generator with an ozone concentration of approximately 5000 ppm.

X-ray diffraction

θ - 2θ measurements were acquired on a PANalytical X'Pert 2 Pro.

X-ray absorption

X-ray absorption measurements were performed at beamline 10-1 at Stanford Synchrotron Radiation Lightsource. Data were taken in total electron yield mode with 45-degree x-ray incidence and 1 mm² beam size.

Transport measurements

Gold contacts of 30 nm thickness were evaporated onto the samples in van der Pauw geometry then aluminum wires were ultrasonically bonded. 4-point transport measurements were carried out in a ⁴He cryostat.

Scanning transmission electron microscopy

TEM specimen lamellae from as-grown samples (Fig. 4(a, b, e, f)) were prepared using a focused ion beam (FIB) Helios 5 UX. Scanning transmission electron microscopy (STEM) images of as-grown samples (Fig. 4(a, b)) were recorded using a double-corrected Thermo Fisher SPECTRA 300 operated at 200 kV using a convergence semi-angle of 20 mrad and a beam current of 50 pA. Energy loss spectrum images were acquired using a continuum spectrometer equipped with a direct electron detection K3 camera from Gatan. A four quadrant

Super-X windowless silicon drift detector system was used to acquire the energy dispersive x-ray spectroscopy (EDX) signal. The EDX maps were generated using the Thermo Fisher Scientific Velox software following the Cliff-Lorimer approach with Brown-Powell ionization cross-section models.

STEM characterization of a capped, ozone-annealed sample (Fig. 4(c)) was performed on a cross-sectional lamella prepared with the standard FIB lift-out procedure using a Thermo Fisher Helios G4 UX FIB. ADF-STEM imaging was performed on aberration-corrected TFS Titan Themis 300 operating at 300 kV with probe convergence semi-angle of 30 mrad.

STEM samples of the oxygen annealed uncapped sample were prepared by milling out and mounting a lamella onto a copper grid using a Thermo Fisher Scientific Helios 5 CX Dual Beam FIB scanning electron microscope (SEM), with gallium as the source. The lamella was then thinned using a Thermo Scientific Helios 5 Hydra UX Dual Beam plasma FIB to mitigate damage caused by the harsher gallium-ion beam. High-angle annular dark field images were acquired on a JEOL Neo-ARM operating at 200 kV with a nominally 30 mrad convergence semi-angle and 16 μ s dwell time. To minimize beam damage to the region of interest the electron beam was first focused on the sample in a sacrificial region of the substrate, the stage was then moved to the film and immediately blanked to allow for the stage to settle without damaging the sample. The beam was then un-blanked at a high magnification with a small focus region selected, which was rapidly focused, and then the magnification decreased, which minimized the region of the sample that incurred significant damage. Images with increased magnification were then acquired.

Density functional theory

We perform first-principles density functional calculations within the Perdew–Burke–Ernzerhof exchange–correlation functional revised for solid (PBEsol)³⁵ as implemented in the Vienna *Ab initio* Simulation Package (VASP) with the projector augmented wave (PAW) method^{36–41}. The core and valence electrons are treated using the following electronic configurations: 4s²4p⁶5s² (Sr), 3d⁷4s¹ (Fe), 2s²2p⁴ (O), and a 600 eV plane wave cutoff. Calculations were carried out using the experimental lattice parameters, while internal distortions were neglected since none are observed experimentally. To account for the electronic consequences of oxygen vacancies, we adopt a background-charge approach that varies the total electron number, effectively simulating carrier doping with a uniform compensating background to ensure charge neutrality.

ACKNOWLEDGMENTS

The work at SLAC/Stanford was supported by the US Department of Energy, Office of Basic Energy Sciences, Division of Materials Sciences and Engineering, under contract no. DE-AC02-76SF00515. Part of this work was performed at the Stanford Nano Shared Facilities (SNSF) RRID:SCR_023230, supported by the National Science Foundation under award

ECCS-2026822. Authors acknowledge the use of instrumentation as well as the technical advice provided by the Joint Electron Microscopy Center at ALBA (JEMCA) and funding from Grant IU16-014206 (METCAM-FIB) to ICN2 funded by the European Union through the European Regional Development Fund (ERDF), with the support of the Ministry of Research and Universities, Generalitat de Catalunya. Authors acknowledge F. Belarre and M. Rosado from ICN2 for the FIB lamellae preparation of the as-grown samples. STEM HAADF imaging using the Neo-ARM was supported by the Center for Nanophase Materials Sciences, (CNMS), which is a DOE Office of Science User Facility using instrumentation within ORNL's Materials Characterization Core provided by UT-Battelle, LLC, under Contract No. DE-AC05-00OR22725 with the DOE. W.J.K. acknowledges funding by the 2024 BK21 FOUR Program of Pusan National University and National Research Foundation (NRF) of Korea (No. RS-2024-00404737). LB acknowledges Dr. Jinkwon Kim's contribution in reoxidizing the samples for electron microscopy measurements at Cornell. The authors acknowledge the support and advice of the late Professor Lena F. Kourkoutis to this study.

DATA AVAILABILITY STATEMENT

The data that support the findings of this study will be available after acceptance in a Dryad repository at [http://doi.org/\[doi\]](http://doi.org/[doi]), reference number [reference number].

- ¹T. Takeda, Y. Yamaguchi, and H. Watanabe, "Magnetic Structure of SrFeO₃," *Journal of the Physical Society of Japan* **33**, 967 (1972).
- ²S. Ishiwata, M. Tokunaga, Y. Kaneko, D. Okuyama, Y. Tokunaga, S. Wakimoto, K. Kakurai, T. Arima, Y. Taguchi, and Y. Tokura, "Versatile helimagnetic phases under magnetic fields in cubic perovskite SrFeO₃," *Physical Review B* **84**, 054427 (2011).
- ³S. Ishiwata, T. Nakajima, J. H. Kim, D. S. Inosov, N. Kanazawa, J. S. White, J. L. Gavilano, R. Georgii, K. M. Seemann, G. Brandl, P. Manuel, D. D. Khalyavin, S. Seki, Y. Tokunaga, M. Kinoshita, Y. W. Long, Y. Kaneko, Y. Taguchi, T. Arima, B. Keimer, and Y. Tokura, "Emergent topological spin structures in the centrosymmetric cubic perovskite SrFeO₃," *Physical Review B* **101**, 134406 (2020).
- ⁴R. Islam, P. Li, M. Beg, M. Sachdev, and G. X. Miao, "Helimagnet-based nonvolatile multi-bit memory units," *Applied Physics Letters* **122**, 152407 (2023).
- ⁵C. Psaroudaki, E. Peraticos, and C. Panagopoulos, "Skyrmion qubits: Challenges for future quantum computing applications," *Applied Physics Letters* **123**, 260501 (2023).
- ⁶Y. Takeda, K. Kanno, T. Takada, O. Yamamoto, M. Takano, N. Nakayama, and Y. Bando, "Phase Relation in the Oxygen Nonstoichiometric System SrFeO_x (2.5 ≤ x ≤ 3.0)," *Journal of Solid State Chemistry* **63**, 237–249 (1986).
- ⁷M. Schmidt, "Composition adjustment of non-stoichiometric strontium ferrite SrFeO_{3-δ}," *Journal of Physics and Chemistry of Solids* **61**, 1363–1365 (2000).
- ⁸L. Wang, Z. Yang, J. Wu, M. E. Bowden, W. Yang, A. Qiao, and Y. Du, "Time- and strain-dependent nanoscale structural degradation in phase change epitaxial strontium ferrite films," *npj Materials Degradation* **4**, 3–8 (2020).
- ⁹E. Enriquez, A. Chen, Z. Harrell, X. Lü, P. Dowden, N. Koskelo, M. Janoschek, C. Chen, and Q. Jia, "Oxygen vacancy-driven evolution of structural and electrical properties in SrFeO_{3-δ} thin films and a method of stabilization," *Applied Physics Letters* **109**, 141906 (2016).
- ¹⁰V. R. Nallagatla, T. Heisig, C. Baeumer, V. Feyer, M. Jugovac, G. Zamborlini, C. M. Schneider, R. Waser, M. Kim, C. U. Jung, and R. Dittmann, "Topotactic Phase Transition Driving Memristive Behavior," *Advanced Materials* **31**, 1903391 (2019).
- ¹¹C. Ge, C.-x. Liu, Q.-l. Zhou, Q.-h. Zhang, J.-y. Du, J.-k. Li, C. Wang, L. Gu, G.-z. Yang, and K.-j. Jin, "A Ferrite Synaptic Transistor with Topotactic Transformation," *Advanced Materials* **31**, 1900379 (2019).
- ¹²J. Fowlie, J. Li, D. Puggioni, L. Barreto, L. D. Yuan, J. M. Rondinelli, R. Sutarto, T. D. Boyko, F. Orlandi, P. Manuel, D. Khalyavin, E. G. Lomeli, B. Moritz, T. P. Devereaux, S. Koroluk, R. J. Green, S. J. May, and H. Y. Hwang, "Biaxial Strain Control of Helimagnetism via Chemical Expansion in Thin Film SrFeO₃," *arXiv cond-mat*, 2602.10372v2 (2026).
- ¹³D. Mateika, H. Kohler, H. Laudan, and E. VölkeI, "Mixed-perovskite substrates for high-T_c superconductors," *Journal of Crystal Growth* **109**, 447–456 (1991).
- ¹⁴J. B. MacChesney, R. C. Sherwood, and J. F. Potter, "Electric and magnetic properties of the strontium ferrates," *The Journal of Chemical Physics* **43**, 1907–1913 (1965).
- ¹⁵M. Reehuis, C. Ulrich, A. Maljuk, C. Niedermayer, B. Ouladdiaf, A. Hoser, T. Hofmann, and B. Keimer, "Neutron diffraction study of spin and charge ordering in SrFeO_{3-δ}," *Physical Review B* **85**, 184109 (2012).
- ¹⁶H. Ikeno, I. Tanaka, T. Miyamae, T. Mishima, H. Adachi, and K. Ogasawara, "First principles calculation of Fe L_{2,3}-edge X-ray absorption near edge structures of iron oxides," *Materials Transactions* **45**, 1414–1418 (2004).
- ¹⁷N. Hayashi, T. Terashima, and M. Takano, "Oxygen-holes creating different electronic phases in Fe⁴⁺-oxides: Successful growth of single crystalline films of SrFeO₃ and related perovskites at low oxygen pressure," *Journal of Materials Chemistry* **11**, 2236–2238 (2001).
- ¹⁸H. Yamada, M. Kawasaki, and Y. Tokura, "Epitaxial growth and valence control of strained perovskite SrFeO₃ films," *Applied Physics Letters* **80**, 622–624 (2002).
- ¹⁹S. Chakraverty, T. Matsuda, H. Wadati, J. Okamoto, Y. Yamasaki, H. Nakao, Y. Murakami, S. Ishiwata, M. Kawasaki, Y. Taguchi, Y. Tokura, and H. Y. Hwang, "Multiple helimagnetic phases and topological Hall effect in epitaxial thin films of pristine and Co-doped SrFeO₃," *Physical Review B* **88**, 220405(R) (2013).
- ²⁰D. Hong, C. Liu, J. Pearson, and A. Bhattacharya, "Epitaxial growth of high quality SrFeO₃ films on (001) oriented (LaAlO₃)_{0.3}(Sr₂TaAlO₆)_{0.7}," *Applied Physics Letters* **111**, 232408 (2017).
- ²¹P. C. Rogge, R. J. Green, R. Sutarto, and S. J. May, "Itinerancy-dependent noncollinear spin textures in SrFeO₃, CaFeO₃, and CaFeO₃/SrFeO₃ heterostructures probed via resonant X-ray scattering itinerancy-dependent noncollinear spin," *Physical Review Materials* **3**, 084404 (2019).
- ²²M. Onose, H. Takahashi, H. Sagayama, Y. Yamasaki, and S. Ishiwata, "Complete phase diagram of Sr_{1-x}La_xFeO₃ with versatile magnetic and charge ordering," *Physical Review Materials* **4**, 114420 (2020).
- ²³O. I. Lebedev, J. Verbeeck, G. V. Tendeloo, N. Hayashi, and T. Terashima, "Structure and microstructure of epitaxial Sr_nFe_nO_{3n-1} films," *Philosophical Magazine* **84**, 3825 (2004).
- ²⁴Y. Xing, I. Kim, K. T. Kang, J. Byun, W. S. Choi, J. Lee, and S. H. Oh, "Monitoring the formation of infinite-layer transition metal oxides through in situ atomic-resolution electron microscopy," *Nature Chemistry* **17**, 66 (2024).
- ²⁵N. Jiang, "Electron beam damage in oxides : a review," *Reports on Progress in Physics* **79**, 016501 (2016).
- ²⁶A. Khare, J. Lee, J. Park, G. Y. Kim, S. Y. Choi, T. Katase, S. Roh, T. S. Yoo, J. Hwang, H. Ohta, J. Son, and W. S. Choi, "Directing Oxygen Vacancy Channels in SrFeO_{2.5} Epitaxial Thin Films," *ACS Applied Materials and Interfaces* **10**, 4831–4837 (2018).
- ²⁷R. J. Green and G. A. Sawatzky, "Negative Charge Transfer Energy in Correlated Compounds," *Journal of the Physical Society of Japan* **93**, 121007 (2024).
- ²⁸P. C. Rogge, P. Shafer, G. Fabbris, W. Hu, E. Arenholz, E. Karapetrova, M. P. M. Dean, R. J. Green, and S. J. May, "Depth-Resolved Modulation of Metal – Oxygen Hybridization and Orbital Polarization across Correlated Oxide Interfaces," *Advanced Materials* **31**, 1902364 (2019).
- ²⁹D. Takegami, M. Nakamura, A. Melendez-Sans, K. Fujinuma, R. Nakamura, M. Yoshimura, K. D. Tsuei, A. Tanaka, M. Gen, Y. Tokunaga, S. Ishiwata, and T. Mizokawa, "Negative charge-transfer energy in SrFeO₃ revisited with hard x-ray photoemission spectroscopy," *Physical Review B* **109**, 235138 (2024).

- ³⁰S. Caspi, L. Shoham, M. Baskin, and K. Weinfeld, "The effect of capping layers on the near-surface region of SrVO₃ films," *Journal of Vacuum Science and Technology A: Vacuum, Surfaces, and Films* **40**, 013208 (2022).
- ³¹M. Mezhoud, M. Rath, S. Gascoin, S. Duprey, P. Marie, J. Cardin, C. Labbé, W. Prellier, and U. Lüders, "Nanoscale generation perovskite-based TCOs using binary and ternary oxides capping layers," *Nanoscale* **17**, 15319–15330 (2025).
- ³²P. Salg, L. Zeinar, A. Radetinac, D. Walk, H. Maune, R. Jakoby, L. Alff, and P. Komissinskiy, "Oxygen diffusion barriers for epitaxial thin-film heterostructures with highly conducting SrMoO₃ electrodes," *Journal of Applied Physics* **127**, 065302 (2020).
- ³³M. Kubicek, Z. Cai, W. Ma, B. Yildiz, H. Hutter, and J. Fleig, "Tensile Lattice Strain Accelerates Oxygen Surface Exchange and diffusion in La_{1-x}Sr_xCoO_{3-δ} thin films," *ACS Nano* **7**, 3276–3286 (2013).
- ³⁴L. Iglesias, A. Gomez, M. Gich, and F. Rivadulla, "Tuning Oxygen Vacancy Diffusion through Strain in SrTiO₃ Thin Films," *ACS Applied Materials and Interfaces* **10**, 35367 (2018).
- ³⁵J. P. Perdew, A. Ruzsinszky, G. I. Csonka, O. A. Vydrov, G. E. Scuseria, L. A. Constantin, X. Zhou, and K. Burke, "Restoring the density-gradient expansion for exchange in solids and surfaces," *Physical Review Letters* **100**, 136406 (2008).
- ³⁶G. Kresse and J. Hafner, "Ab initio molecular dynamics for liquid metals," *Physical Review B* **47**, 558–561 (1993).
- ³⁷G. Kresse and J. Furthmüller, "Efficiency of ab-initio total energy calculations for metals and semiconductors using a plane-wave basis set," *Computational Materials Science* **6**, 15–50 (1996).
- ³⁸G. Kresse and J. Furthmüller, "Efficient iterative schemes for ab initio total-energy calculations using a plane-wave basis set," *Physical Review B* **54**, 11169–11186 (1996).
- ³⁹J. P. Perdew, K. Burke, and M. Ernzerhof, "Generalized gradient approximation made simple," *Physical Review Letters* **77**, 3865–3868 (1996).
- ⁴⁰P. E. Blöchl, "Projector augmented-wave method," *Physical Review B* **50**, 17953–17979 (1994).
- ⁴¹G. Kresse and D. Joubert, "From ultrasoft pseudopotentials to the projector augmented-wave method," *Physical Review B* **59**, 1758–1775 (1999).